• Original Paper •

Hybrid Methods for Computing the Streamfunction and Velocity Potential for Complex Flow Fields over Mesoscale Domains

Jie CAO[1,2], Qin XU[*3], Haishan CHEN[1], and Shuping MA[4]

[1]*Key Laboratory of Meteorological Disaster (KLME), Ministry of Education & Collaborative Innovation Center on Forecast and Evaluation of Meteorological Disasters (CIC-FEMD), Nanjing University of Information Science & Technology, Nanjing 210044, China*

[2]*Cooperative Institute for Mesoscale Meteorological Studies (CIMMS), University of Oklahoma, Norman 73072, Oklahoma, USA*

[3]*NOAA/OAR/National Severe Storms Laboratory, Norman 73069, Oklahoma, USA*

[4]*Institute of Atmospheric Physics, Chinese Academy of Sciences, Beijing 100029, China*

ABSTRACT

Three types of previously used numerical methods are revisited for computing the streamfunction ψ and velocity potential χ from the horizontal velocity $\boldsymbol{v}$ in limited domains. The first type, called the SOR-based method, uses a classical successive over-relaxation (SOR) scheme to compute ψ (or χ) first with an arbitrary boundary condition (BC) and then χ (or ψ) with the BC derived from $\boldsymbol{v}$. The second type, called the spectral method, uses spectral formulations to construct the inner part of (ψ, χ)—the inversion of (vorticity, divergence) with a homogeneous BC, and then the remaining harmonic part of (ψ, χ) with BCs from $\boldsymbol{v}$. The third type, called the integral method, uses integral formulas to compute the internally induced (ψ, χ)—the inversion of domain-internal (vorticity, divergence) using the free-space Green's function without BCs and then the remaining harmonic ψ (or χ) with BCs from $\boldsymbol{v}$ minus the internally-induced part. Although these methods have previously been successfully applied to flows in large-scale and synoptic-scale domains, their accuracy is compromised when applied to complex flows over mesoscale domains, as shown in this paper. To resolve this problem, two hybrid approaches, the integral-SOR method and the integral-spectral method, are developed by combining the first step of the integral method with the second step adopted from the SOR-based and spectral methods, respectively. Upon testing these methods on real-case complex flows, the integral-SOR method is significantly more accurate than the integral-spectral method, noting that the latter is still generally more accurate than the three previously-used methods. The integral-SOR method is recommended for future applications and diagnostic studies of complex flows.

Key words: streamfunction and velocity potential, complex flow fields, successive over-relaxation method, mesoscale study

Article Highlights:

- Significant losses in accuracy result when previous methods were applied to compute the streamfunction and velocity potential for complex flows over mesoscale domains.
- Three previous methods are revisited to determine their strengths and weaknesses.
- Two hybrid methods are constructed with improved accuracies.
- The integral-SOR method is recommended for future applications.

---

1. Introduction

It is well-known that a horizontal velocity field can be partitioned into rotational and divergent components that

---

* Corresponding author: Qin XU
  Email: Qin.Xu@noaa.gov

are represented by a streamfunction ψ and a velocity potential χ, respectively. This kind of flow partitioning has been useful in studying atmospheric-flow transformations and energy cascades (DiMego and Bosart, 1982; Vallis et al., 1997), in developing vorticity-based models for oceanic-flow simulations, in numerical weather prediction (Haltiner and Williams, 1980; Allen et al., 1990; Jung and Arakawa, 2008), and in choosing control variables, formulating constraints, constructing and estimating background error covariance functions for data analyses and assimilation (Hollingsworth and Lönnberg, 1986; Daley, 1991; Xu and Qiu, 1994; Xu and Wei, 2001, 2002; Mewes and Shapiro, 2002; Xu, 2021). It has long been recognized that the solution of (ψ, χ) is unique in an unbounded or periodic domain but not in a limited domain (Sangster, 1960; Lynch, 1989; Chen and Kuo, 1992a, b; Li et al., 2006; Xu et al., 2011). Although global wind data are becoming denser and easier to access than decades ago, their spatial resolutions are still too coarse for mesoscale domains; and the data-set sizes will be too large if ψ and χ are computed over a periodic global domain, only to be locally used for mesoscale studies. This justifies the need for flow decompositions in limited domains.

The non-uniqueness of (ψ, χ) in a limited domain is caused by the existence of the harmonic components of (ψ, χ) in the null space of the coupled system of equations and boundary conditions in a limited domain (see section 2 and Appendix A of Xu et al., 2011). To avoid such non-uniqueness, Sangster (1960) proposed a method with the harmonic component represented solely by ψ, and Lynch (1989) formulated eight variants of Sangster's method with the horizontal velocity partitioned into three mutually orthogonal components, that is, the rotational, divergent, and harmonic components. Since the classical successive over-relaxation (SOR) scheme was used in Sangster's method (and its variants) to solve for (ψ, χ) from their respective Poisson equations with associated boundary conditions, the Sangster's method is, therefore, a SOR-based method. By using sine and cosine series expansions, Chen and Kuo (1992a, b; CK92a, b hereafter) developed two versions of the spectral method (called the S-version and C-version, respectively, hereafter) for computing (ψ, χ) in a limited domain. In CK92b, the C-version was shown to be more accurate and efficient than the S-version, but two solvability conditions were overlooked in the C-version (see the related exposition in section 2.3 of this paper). In considering a two-component partitioning of (ψ, χ) in a limited domain, one component of (ψ, χ) is induced purely internally and uniquely by the vorticity and divergence inside the domain. The remaining component of (ψ, χ) is taken as a harmonic one because it is induced purely externally and non-uniquely by unknown vorticity and divergence fields outside the domain.

Xu et al. (2011) and Cao and Xu (2011, CX11 hereafter) developed a method based on integral formulas, called the integral method hereafter, for computing the internally and externally induced (ψ, χ) in a limited domain of arbitrary shape. The integral method was used recently by Xu and Cao (2021) to solve the nonlinear balance equation iteratively

over limited domains and found this approach to be more accurate and efficient than the classical SOR-based scheme in solving the boundary value problem associated with the Poisson equation.

The three previous methods have been applied to various velocity fields in diagnostic studies of weather systems (Buechler and Fuelberg, 1986; Loughe et al., 1995; Fiedler, 2002; Aimi et al., 2014; Cao et al., 2019; You and Fung, 2019; You et al., 2019; Ullah et al., 2020, 2021; Cao, 2021; Fu et al., 2021; Zhao and Cook, 2021) and in data assimilation (Daley, 1991; Parrish and Derber, 1992; Xu et al., 2006, 2007). In these applications, the flow structures of concern are well covered by sufficiently large analysis domains and can be accurately partitioned by the integral method. In other words, the partitioned velocity fields computed from (ψ, χ) can reconstruct the original velocity fields with high accuracy. However, as we noted recently from some applications of the integral method to strong and complex flow fields during a torrential blizzard event in mesoscale studies, this method tends to lose considerable accuracy, although the integral method is still more accurate than the SOR-based and spectral methods. The accuracy further deteriorates under stronger and more heterogenous flow, exhibiting sharp variations not only inside the domain but also across or along the domain boundary. In this case, the sum of the partitioned velocities cannot accurately recover the original velocity, so the concerned flow field is not accurately partitioned for diagnostic studies. This problem is new and unresolved for all the three previous methods, as shown in this paper.

This paper aims to solve or alleviate the abovementioned new problem by optimally combining the previous methods. To achieve this, we will revisit the three previous methods to identify each method's strengths (or weaknesses) which can be retained (or avoided) via a hybrid approach to reduce the aforementioned loss of accuracy in mesoscale applications. This paper shows that the SOR-based and spectral methods tend to lose their accuracy because of increased spatial variations of the original velocities inside the domain. In contrast, the integral method tends to lose its accuracy due mainly to increased variations of original velocity across or along the domain boundary, which reduces the accuracy of the externally induced (ψ, χ) obtained in the second step. Meanwhile, the internally induced (ψ, χ), obtained using Green's functions in the first step, remains sufficiently accurate despite increased spatial variations of velocity inside the domain. The above-highlighted strengths and weaknesses for each method imply that it is possible to construct a new hybrid method by using the integral method first to obtain the internally induced component of (ψ, χ) and then using the SOR-based method or spectral method to obtain the externally induced harmonic component of (ψ, χ). Such hybrid methods will be constructed and tested against the three previous methods with the aforementioned difficult cases recently encountered in mesoscale applications.

The paper is organized as follows. The next section reviews the problem of solving for (ψ, χ) in a limited

domain with the three previous methods revisited in the first three subsections and the two hybrid methods proposed in the last subsection. Section 3 describes the test case and evaluation methods. Section 4 outlines the test experiments, examines the test results from the hybrid methods, and compares these to the results from the previous three methods. Section 5 presents the conclusions.

2. Revisiting the previous methods and design of new hybrid methods

When the horizontal velocity $\boldsymbol{v} = (u, v)$ is represented by (ψ, χ), we have $\boldsymbol{v} = \boldsymbol{k} \times \nabla\psi + \nabla\chi$, where $\boldsymbol{k}$ is the unit vector in the vertical direction and ∇ is the gradient operator in the two-dimensional space of $\boldsymbol{x} \equiv (x, y)$. As mentioned in the introduction section, (ψ, χ) contains no harmonic component in an unbounded or periodic domain, so (ψ, χ) can be uniquely defined by uniquely relating $\boldsymbol{k} \times \nabla\psi$ and $\nabla\chi$ to the rotational and divergent parts of $\boldsymbol{v}$, respectively. In a limited domain, (ψ, χ) contain a harmonic component and thus cannot be uniquely defined and determined due to the nonunique partition and attribution of the harmonic component to (ψ, χ). In this case, the following relationships hold:

$$\nabla^2\psi = \zeta \quad (\text{in } D),\tag{1a}$$

$$\nabla^2\chi = \alpha \quad (\text{in } D),\tag{1b}$$

$$\partial_n\psi + \partial_s\chi = v_s \quad (\text{on } S),\tag{2a}$$

$$\partial_n\chi - \partial_s\psi = v_n \quad (\text{on } S),\tag{2b}$$

where $\zeta = \boldsymbol{k} \cdot \nabla\times\boldsymbol{v} = \partial_x v - \partial_y u$ is the vorticity, $\alpha = \nabla \cdot \boldsymbol{v} = \partial_x u + \partial_y v$ is the divergence, D denotes the limited domain, S denotes the boundary of D, ∂_n (or ∂_s) denotes the boundary-normal (or boundary-tangential) component of ∇, and v_n (or v_s) is the boundary-normal (or boundary-tangential) component of $\boldsymbol{v}$ on S.

Applying the Gauss and Stokes's theorems to Eqs. (1) and (2) leads to the following solvability conditions:

$$\int_S v_s \mathrm{d}l = \int_D \zeta \mathrm{d}\boldsymbol{x},\tag{3a}$$

$$\int_S v_n \mathrm{d}l = \int_D \alpha \mathrm{d}\boldsymbol{x},\tag{3b}$$

where $\int_S (\ )\mathrm{d}l$ denotes the line-integration of $(\ )$ along the closed loop of S and $\int_D (\ )\mathrm{d}\boldsymbol{x}$ denotes the area-integration of $(\ )$ over D. These two solvability conditions are accurately satisfied in discrete forms by the original $\boldsymbol{v}$ fields used in this paper in three mesoscale domains (as shown later in Table 2) but not accurately by the reconstructed velocity fields (as shown later in Table 3).

The above two solvability conditions can be expressed in terms of (ψ, χ). In this case, each solvability condition can be split into two parts as shown below. Since (ψ, χ) are single-valued continuous functions along the closed loop of S, the first part of the solvability condition in Eq. (3a) or (3b) in terms of (ψ, χ) satisfies:

$$\int_S \partial_s\chi \mathrm{d}l = \int_S \mathrm{d}\chi = 0,\tag{4a}$$

$$\int_S \partial_s\psi \mathrm{d}l = \int_S \mathrm{d}\psi = 0.\tag{4b}$$

The remaining second part of the solvability condition can be then obtained by substituting Eqs. (2a) and (4a) [or (2b) and (4b)] into Eq. (3a) [or (3b)], which gives

$$\int_S \partial_n\psi \mathrm{d}l = \int_S v_s \mathrm{d}l = \int_D \zeta \mathrm{d}\boldsymbol{x},\tag{5a}$$

$$\int_S \partial_n\chi \mathrm{d}l = \int_S v_n \mathrm{d}l = \int_D \alpha \mathrm{d}\boldsymbol{x}.\tag{5b}$$

2.1. Integral method

In the integral method, the internally induced (ψ, χ), denoted by $(\psi_{\text{in}}, \chi_{\text{in}})$, is given by

$$[\psi_{\text{in}}(\boldsymbol{x}), \chi_{\text{in}}(\boldsymbol{x})] = (2\pi)^{-1}\int_D \mathrm{d}\boldsymbol{x}'[\zeta(\boldsymbol{x}'), \alpha(\boldsymbol{x}')]\ln r,\tag{6}$$

where $r = |\boldsymbol{x}' - \boldsymbol{x}|$ and $(2\pi)^{-1}\ln r$ is the free-space Green's function for Poisson equation in an unbounded domain but here it is applied to (ζ, α) in D. Three discretization schemes were developed in CX11 for computing the integral in Eq. (6), and the first scheme that used a staggered grid for (ζ, α) is used in this paper. Ideally, $(\psi_{\text{in}}, \chi_{\text{in}})$ should exactly satisfy those solvability conditions that are further partitioned from Eqs. (4) and (5), that is,

$$\int_S \partial_s(\psi_{\text{in}}, \chi_{\text{in}})\mathrm{d}l = 0,\tag{7a}$$

$$\int_S \partial_n(\psi_{\text{in}}, \chi_{\text{in}})\mathrm{d}l = \int_S (v_s, v_n)\mathrm{d}l = \int_D (\zeta, \alpha)\mathrm{d}\boldsymbol{x}.\tag{7b}$$

Practically, the computed $(\psi_{\text{in}}, \chi_{\text{in}})$ cannot accurately satisfy the second solvability condition in Eq. (7b) due mainly to discretization errors in computing $\partial_n(\psi_{\text{in}}, \chi_{\text{in}})$, although the first solvability condition in Eq. (7a) is exactly satisfied. The errors involved are usually small and negligible. Still, they can increase significantly as the original $\boldsymbol{v}$ becomes strong with sharp variations across or along S (as mentioned in the introduction and seen later from Tables 3 and 4). Note that Green's function in Eq. (6) involves no boundary condition, and the derived integral form of $(\psi_{\text{in}}, \chi_{\text{in}})$ is simple and unaffected by any complications in the boundary condition. Owing to the simplicity of this integral form and the use of a staggered grid in discretizing (ζ, α), the computed

$(\psi_{\mathrm{in}}, \chi_{\mathrm{in}})$ is more accurate and less sensitive to increased and sharpened spatial variations of original v in D than the solutions computed by the other two methods. This is an important strength of the integral method that should be adopted for the purpose of first obtaining $(\psi_{\mathrm{in}}, \chi_{\mathrm{in}})$ in a hybrid approach.

The remaining externally induced harmonic component of (ψ, χ), denoted by $(\psi_{\mathrm{e}}, \chi_{\mathrm{e}})$, is computed in the second step by simply setting $\chi_{\mathrm{e}} = 0$. With $\chi_{\mathrm{e}} = 0$, (ψ, χ) can be uniquely defined by relating $\boldsymbol{k} \times \nabla\psi$ (or $\nabla\chi$) to the nondivergent (or divergent) part of v, where the nondivergent part consists of the rotational part and harmonic part of v. With the above simplification, four discretization schemes were developed in CX11 for computing ψ_{e} and the Cauchy-integral scheme (shown in section 4 of CX11) is used in this paper. This scheme computes the complex velocity potential defined by $\omega_{\mathrm{e}} = \varphi_{\mathrm{e}} - i\psi_{\mathrm{e}}$ where i is the imaginary unit, while the boundary value of ψ_{e} (or φ_{e}) is obtained by integrating $\partial_s\psi_{\mathrm{e}} = v_{n,\mathrm{in}} - v_n$ (or $\partial_s\varphi_{\mathrm{e}} = v_s - v_{s,\mathrm{in}}$) along S as shown in (3.9) [or (3.10)] of Xu et al. (2011), where $v_{n,\mathrm{in}}$ (or $v_{s,\mathrm{in}}$) is the boundary-normal (or boundary-tangential) component of $v_{\mathrm{in}} \equiv \boldsymbol{k} \times \nabla\psi_{\mathrm{in}} + \nabla\chi_{\mathrm{in}}$ on S. Since $\nabla^2(\psi_{\mathrm{e}}, \varphi_{\mathrm{e}}) = (0, 0)$ and $\partial_s(\psi_{\mathrm{e}}, \varphi_{\mathrm{e}}) = \partial_n(-\varphi_{\mathrm{e}}, \psi_{\mathrm{e}})$ on S according to the Cauchy-Riemann conditions, the paired solvability conditions for $(\psi_{\mathrm{e}}, \varphi_{\mathrm{e}})$ can be derived from the partitioned solvability conditions in Eqs. (7a, b) in the following form:

$$\int_S \partial_s(\psi_{\mathrm{e}}, \varphi_{\mathrm{e}})\mathrm{d}l = \int_S \partial_n(-\varphi_{\mathrm{e}}, \psi_{\mathrm{e}})\mathrm{d}l$$
$$= \int_S (v_{n,\mathrm{in}} - v_{\mathrm{in}}, v_s - v_{s,\mathrm{in}})\mathrm{d}l = (0, 0) . \quad (8)$$

Note from Eqs. (2a, b) that $v_{s,\mathrm{in}} = \partial_n\psi_{\mathrm{in}} + \partial_s\chi_{\mathrm{in}}$ and $v_{n,\mathrm{in}} = \partial_n\chi_{\mathrm{in}} - \partial_s\psi_{\mathrm{in}}$ on S, so the solvability conditions in Eq. (8) can be exactly satisfied only if $(\psi_{\mathrm{in}}, \chi_{\mathrm{in}})$ exactly satisfies the solvability conditions in Eqs. (7a, b). As explained earlier, for $(\psi_{\mathrm{in}}, \chi_{\mathrm{in}})$ computed in the first step, the paired solvability conditions in Eq. (7a) are satisfied exactly, but the paired solvability conditions in Eq. (7b) are not; therefore, the paired solvability conditions in Eq. (8) are also not exactly satisfied. Consequently, the boundary value of ψ_{e} (or φ_{e}) obtained by integrating $\partial_n\chi_{\mathrm{in}} - v_n$ (or $v_s - \partial_n\psi_{\mathrm{in}}$) along the boundary loop undergoes a discontinuous jump when the integration returns to the beginning point. Although such a jump can be spread out and somewhat diluted by redistributing it evenly over the entire boundary loop, the paired solvability conditions in Eq. (7b) are still not exactly satisfied, and their induced errors in the computed boundary values of $(\psi_{\mathrm{e}}, \varphi_{\mathrm{e}})$ remain essentially intact. While more accurate than the other three schemes developed in CX11 for computing ψ_{e} (with $\chi_{\mathrm{e}} = 0$), the Cauchy-integral scheme is quite sensitive to small errors in the computed boundary values of $(\psi_{\mathrm{e}}, \chi_{\mathrm{e}})$ that cannot accurately satisfy the paired solvability conditions in Eq. (8), because the scheme is derived from an analytical integral and this integral requires the paired solvability conditions in Eq. (8) to be precisely satisfied. This appears to be a weakness for the integral method. Still, it can be avoided if ψ_{e} (with $\chi_{\mathrm{e}} = 0$) can be computed by another method with an improved accuracy after $(\psi_{\mathrm{in}}, \chi_{\mathrm{in}})$ is obtained by the integral method via a hybrid approach.

2.2. *SOR-based method*

The SOR-based method (Sangster, 1960) solves the coupled system of Eqs. (1)–(2) with either ψ or χ freely prescribed on S. For example, if ψ is chosen to be freely prescribed on S, then ψ can be solved first from Eq. (1a) in D, which gives $\partial_n\psi$ along S. Thus, $\partial_s\chi$ can be obtained along S from Eq. (2a), and integrating $\partial_s\chi$ along S gives the boundary value of χ that allows χ be finally solved from Eq. (1b) in D. In this case, the solvability condition in Eq. (4b) is satisfied exactly, but the solvability condition in Eq. (5a) is satisfied only approximately due to discretization errors in solving for ψ and computing $\partial_n\psi$. Thus, when the boundary value of $\partial_s\chi$ is obtained from Eq. (2a), its boundary loop integral is not exactly zero. In other words, the solvability condition in Eq. (4a) is not exactly satisfied, so the boundary value of χ obtained by integrating $\partial_s\chi$ along S undergoes a discontinuous variation when the loop integration returns to the beginning point.

Similarly but alternatively, if χ is chosen to be freely prescribed on S, with χ solved first from Eq. (1b) in D, then the solvability condition in Eq. (4a) is satisfied exactly, but the solvability condition in Eq. (5b) is satisfied only approximately due to discretization errors in solving for χ and computing $\partial_n\chi$. Thus, when the boundary value of $\partial_s\psi$ is obtained from Eq. (2b), its boundary loop integration is not exactly zero. In this case, the solvability condition in Eq. (4b) is not exactly satisfied and the boundary value of ψ, obtained by integrating $\partial_s\psi$ along S, undergoes a discontinuous jump when the loop integration returns to the beginning point.

The abovementioned jump can be negligibly small if the original v is sufficiently smooth. Still, it can become large if the original v demonstrates sharp variations not adequately resolved by the analysis grid, especially across or along the domain boundary (as shown later in Table 3). Although this jump can be thinned out by redistributing it evenly over the entire boundary loop, its implied error in the boundary condition remains essentially intact.

In this paper, the SOR is implemented with (ψ, χ) and (ζ, α) discretized on the same grid. The discretization errors of $\nabla^2(\psi, \chi)$ and (ζ, α) are large in areas of complex flow, and these large errors tend to accumulate as the iterative process of SOR goes sequentially point-by-point through the areas of complex flow. The SOR-based method is thus relatively sensitive to (and its accuracy can be significantly reduced by) increased spatial variations of original v and thus further sharpened variations of (ζ, α) that were computed from original v inside the domain D (as shown later in section 4). On the other hand, if the SOR-based method is used to solve for $(\psi_{\mathrm{e}}, \chi_{\mathrm{e}})$ with a vanished (ζ, α) inside D, then the discretization errors of $\nabla^2(\psi, \chi)$ and (ζ, α) will become small or much smaller everywhere inside D, so $(\psi_{\mathrm{e}}, \chi_{\mathrm{e}})$ can be solved with improved accuracy. This implies that the SOR-based method should have an advantage if it is used to solve for

the externally induced (ψ_e, χ_e) after the internally induced (ψ_{in}, χ_{in}) is obtained by the integral method via a hybrid approach. Such a hybrid approach will be considered in section 2.4.

2.3. *Spectral method and modified spectral method*

As mentioned in the introduction, the spectral method of CK92a,b has two versions, called the S-version and C-version, respectively. In either version, (ψ, χ) is divided into two parts, called the inner part and harmonic part and denoted by $(\psi_{in,n}, \chi_{in,n})$ and $(\psi_{h,a}, \chi_{h,a})$, respectively. The inner part is well defined in the S-version by the solution of $\nabla^2(\psi_{in,n}, \chi_{in,n}) \equiv (\zeta, \alpha)$ in D with a zero Dirichlet boundary value but is ill-defined in the C-version by the solution of $\nabla^2(\psi_{in,n}, \chi_{in,n}) \equiv (\zeta, \alpha)$ in D with a zero Neumann boundary value [see Eq. (2.7) of CK92b] without considering the two solvability conditions in Eqs. (5a,b). The ill-defined $(\psi_{in,n}, \chi_{in,n})$ in the C-version has not caused significant inconsistency problems in previous applications to synoptic-scale flows in large-scale limited domains in which $\int_D \zeta d\boldsymbol{x}$ and $\int_D \alpha d\boldsymbol{x}$ nearly vanish. Thus, the two solvability conditions in Eqs. (5a,b) can be approximately satisfied with a zero Neumann boundary value. Perhaps because of this, the inconsistency problem of the C-version was not noted or addressed when the S-version was refined (Boyd et al., 2013). This inconsistency problem can become serious for applications of the C-version method to complex flows with increased $\int_D \zeta d\boldsymbol{x}$ and/or $\int_D \alpha d\boldsymbol{x}$ (as seen later from Table 2). In this case, the ill-defined $(\psi_{in,n}, \chi_{in,n})$ in the C-version must be properly redefined, as shown below.

The inner part in the C-version can be properly redefined if it is further divided into two sub-parts, denoted by $(\psi_{in,s}, \chi_{in,s})$ and $(\psi_{in,c}, \chi_{in,c})$, respectively, while $(\psi_{in,s}, \chi_{in,s})$ is well-defined by the solution of $\nabla^2(\psi_{in,s}, \chi_{in,s}) = (\int_D \zeta d\boldsymbol{x}, \int_D \alpha d\boldsymbol{x})$ in D with zero Dirichlet boundary value and $(\psi_{in,c}, \chi_{in,c})$ is well defined by the solution of $\nabla^2(\psi_{in,c}, \chi_{in,c}) = (\zeta - \int_D \zeta d\boldsymbol{x}, \alpha - \int_D \alpha d\boldsymbol{x})$ in D with a zero Neumann boundary value. The spectral formulations derived for the S-version's (or C-version's) inner part in CK92a (or CK92b) can be then used to obtain $(\psi_{in,s}, \chi_{in,s})$ [or $(\psi_{in,c}, \chi_{in,c})$] consistency with the solvability conditions in Eqs. (5a,b). The redefined inner part is thus given by $(\psi_{in,n}, \chi_{in,n}) = (\psi_{in,s}, \chi_{in,s}) + (\psi_{in,c}, \chi_{in,c})$ in the first step. After this, the harmonic part, $(\psi_{h,a}, \chi_{h,a})$, can be obtained in the second step using the spectral formulations derived in CK92b for C-version harmonic part. The C-version spectral method is modified in this way and implemented in this paper. According to CK92b, the C-version spectral method is more accurate and efficient than the S-version. The modified C-version spectral method, called the M-spectral method for short, is more accurate than the two original versions of the spectral method of CK92a, b especially for mesoscale domains, so the M-spectral method is used in this paper.

Like the SOR-based method, the second part of the M-spectral method is also not very sensitive to increased variations of the original $\boldsymbol{v}$ across or along S. However, the first part of the M-spectral method is more sensitive than the SOR-based method to increased spatial variations of the original $\boldsymbol{v}$ inside D. The increased sensitivity is due mainly to the use of a zero Dirichlet (or Neumann) boundary value in defining and solving for $(\psi_{in,s}, \chi_{in,s})$ [or $(\psi_{in,c}, \chi_{in,c})$] that can cause sharp near-boundary variations in the solution poorly resolved by the analysis grid, especially when $(\int_D \zeta d\boldsymbol{x}, \int_D \alpha d\boldsymbol{x})$ is not small or (ζ, α) has sharp near-boundary variations. This is because $(\psi_{in,s}, \chi_{in,s})$ [or $(\psi_{in,c}, \chi_{in,c})$] has a zero Dirichlet (or Neumann) boundary value and thus must have sharp near-boundary variations in the boundary-normal (or boundary-parallel) direction so that $\nabla^2(\psi_{in,s}, \chi_{in,s})$ [or $\nabla^2(\psi_{in,c}, \chi_{in,c})$] can have the same sharp near-boundary variations as (ζ, α) to satisfy the Poisson equation. Poorly resolved near-boundary variations in $(\psi_{in,n}, \chi_{in,n})$ [= $(\psi_{in,s}, \chi_{in,s})$ + $(\psi_{in,c}, \chi_{in,c})$] can generate additional errors in the boundary conditions for $(\psi_{h,a}, \chi_{h,a})$ [see Eqs. (2.11)–(2.15) of CK92b], and these additional errors can propagate and spread throughout the domain when $(\psi_{h,a}, \chi_{h,a})$ is solved iteratively. The above-explained additional errors and their propagation make the M-spectral method less accurate than the SOR-based method for the difficult cases considered in this paper (as shown later in Table 1). However, since the additional errors are generated from $(\psi_{in,n}, \chi_{in,n})$ in the M-spectral method, the second part of the method for obtaining $(\psi_{h,a}, \chi_{h,a})$ should still have an advantage if it is used not in the M-spectral method but in a hybrid method to obtain the externally induced (ψ_e, χ_e) after the internally induced $(\psi_{in,n}, \chi_{in,n})$ is obtained by the integral method; this hybrid approach will also be considered in section 2.4.

2.4. *Hybrid approach*

Two hybrid methods are designed to reduce the increased loss of accuracy caused by increased complexities of the original $\boldsymbol{v}$ field, not only in D but also across or along S. The mathematical foundations for the hybrid methods are the same as the adopted three methods mentioned above. In these two hybrid methods, (ψ, χ) is divided into (ψ_{in}, χ_{in}) and (ψ_e, χ_e) for the internally and externally induced components, respectively, in the same way as in the integral method. To retain the strength and related advantages explained in section 2.1 for the integral method, the internally induced components, (ψ_{in}, χ_{in}), should be calculated in the first step in the same way as that in the integral method. The SOR-based method can be used adaptively for computing the externally induced ψ_e (with $\chi_e = 0$) in the second step as described in section 2.2, while the M-spectral method for computing (ψ_e, χ_e) as described in section 2.3. This approach can improve the accuracy of (ψ_e, χ_e) computed in the second step because (as explained in sections 2.2 and 2.3), these two methods are less sensitive than the integral method to increased variations of original $\boldsymbol{v}$ across or along the domain boundary and their caused errors in solvability conditions and related boundary condition errors. The aforementioned hybrid methods are called the integral-SOR and integral-spectral methods, respectively. The detailed computational procedures of the two hybrid methods are shown in Fig. 1. Test results from these two hybrid methods in computing (ψ, χ)

from original v fields with complex flow patterns in mesoscale domains will be shown in section 4 and compared with the results from three previous methods.

3. Test case and evaluation method

3.1. *Test case*

The severe weather case of a blizzard in Xinjiang Province on 30 November 2018 is chosen from a series of difficult cases recently encountered for mesoscale applications of the previous methods. In this case, wind fields in the lower troposphere showed sharp horizontal variations caused by severe weather over complex terrain. The discrete field of original v used in this paper is from the numerical simulation of this chosen case (Ma et al., 2021) with a 3-km horizontal resolution for the innermost nested model domain that covers a 300 km × 300 km square mesoscale area located between the Ili Valley and North Tianshan Mountain. Specifically, the original v field is taken as the simulated wind field at 2100 UTC on 30 November at the model's terrain-following vertical level about 0.5 km above the ground (2.5 km above the mean sea level). This v field serves as a test example. Similar examples of 2D v fields can be

(a) Obtain the discrete internally induced component (ψ_{in}, χ_{in}) in (7b) via the following process:
1. Compute (ζ, α) in staggered grid points which is by a half of the grid spacing in each direction from (u, v).
2. Construct and compute the following expressions for discrete (ψ_{in}, χ_{in}):
$\chi_{in}(\mathbf{x}_{ij}) = (2\pi)^{-1}\sum_p\sum_q\alpha(\mathbf{x}_{pq})[\ln|(p - i, q - j)| + \ln\delta s]\delta s^2$,
$\psi_{in}(\mathbf{x}_{ij}) = (2\pi)^{-1}\sum_p\sum_q\zeta(\mathbf{x}_{pq})[\ln|(p - i, q - j)| + \ln\delta s]\delta s^2$.

↓

(b) Obtain the discrete externally induced component (ψ_e, χ_e) using SOR-based method via the following process:
1. Set $\chi_e = 0$.
2. Solve the Poisson equation for ψ_e:
$\nabla^2 \psi_e = 0$ in D, with the boundary condition:
$- \partial_s \psi_e = v_n + \partial_s \psi_{in}$ on S.
3. SOR-method is adopted with the following discrete solution in the mth iterative step as:
$\psi_e^{(m+1)} = (\lambda/4)[\psi_e^{(m)}{}_{i+1,j} + \psi_e^{(m+1)}{}_{i-1,j} + \psi_e^{(m)}{}_{i,j+1} + \psi_e^{(m+1)}{}_{i,j-1}] + (1-\lambda)\psi_e^{(m)}{}_{ij}$
4. Iteration stops when the remaining error between two iterative steps are small enough.

(c) Obtain the discrete externally induced component (ψ_e, χ_e) using M-spectral method via the following process:
1. Solve the Poisson equation for (ψ_e, χ_e) with the following boundary conditions as:
$\partial_n\psi_e + \partial_s\chi_e = v_s - (\partial_n\psi_{in} + \partial_s\chi_{in})$,
$\partial_n\chi_e - \partial_s\psi_e = v_n - (\partial_n\chi_{in} - \partial_s\psi_{in})$.
2. Set $\partial_s\chi_e = 0$ along the boundary as the first approximation and obtain $\psi_e^{(0)}$ in the expression of harmonic cosine series as shown in Eq. (4.3) in CK92b.
3. With the calculated $\psi_e^{(0)}$, the Neumann boundary value for $\chi_e^{(0)}$ is obtained by:
$\partial_n\chi_e^{(0)} = v_n - (\partial_n\chi_{in} - \partial_s\psi_{in}) + \partial_s\psi_e^{(0)}$.
Solution for $\chi_e^{(0)}$ is obtained from Eq. (4.4) in CK92b.
4. With the obtained ($\psi_e^{(0)}$, $\chi_e^{(0)}$), the first correction of (ψ_e, χ_e), i.e., ($\Delta\psi_e^{(1)}$, $\Delta\chi_e^{(1)}$), can be derived with renewed boundary conditions. Following CK92a, the nth-order approximations of (ψ_e, χ_e) are expressed as:
$\psi_e^{(n)} = \psi_e^{(0)} + \Delta\psi_e^{(1)} + \Delta\psi_e^{(2)} + ... + \Delta\psi_e^{(n)}$,
$\chi_e^{(n)} = \chi_e^{(0)} + \Delta\chi_e^{(1)} + \Delta\chi_e^{(2)} + ... + \Delta\chi_e^{(n)}$.
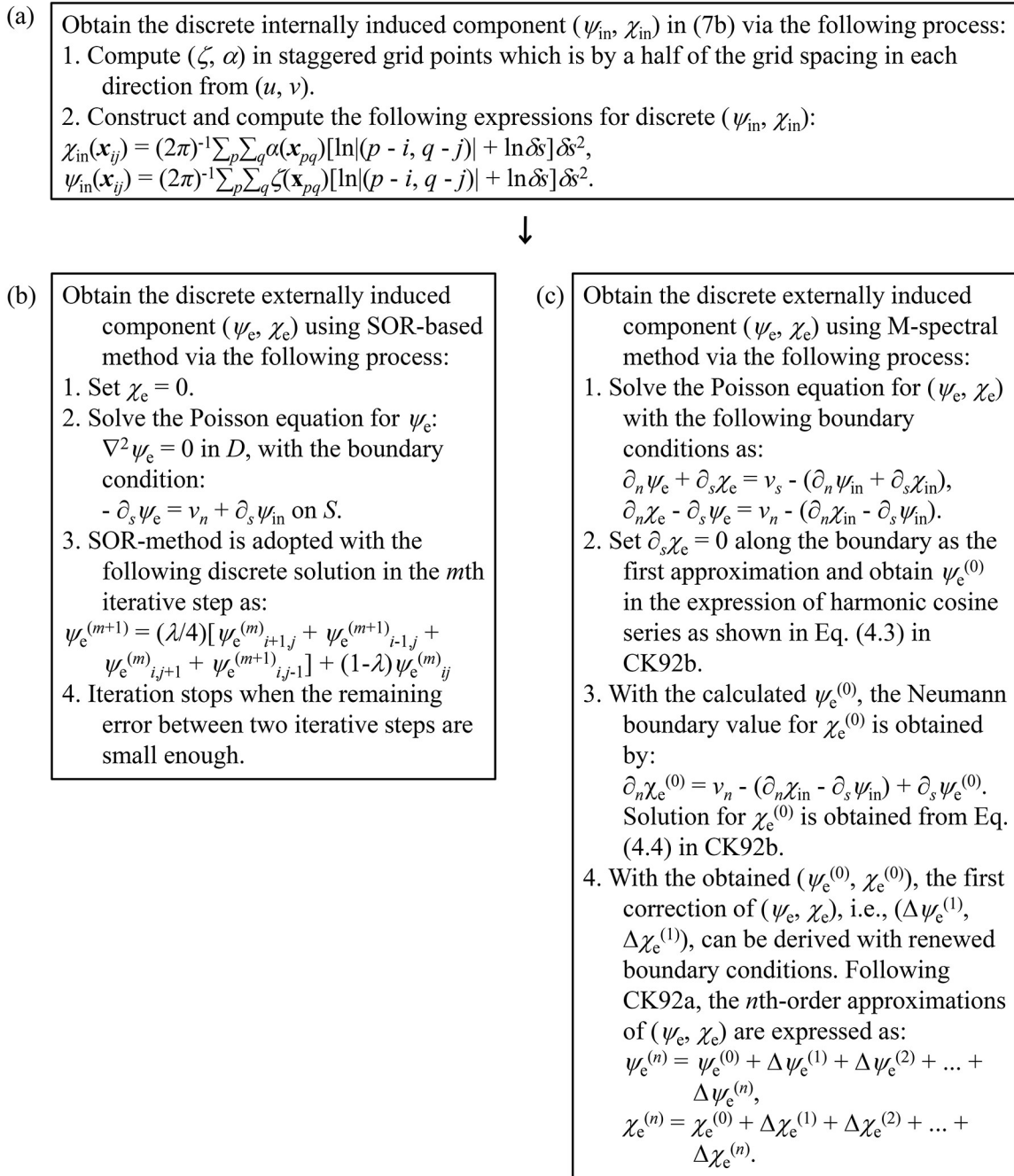
Fig. 1. Computational procedures of (a) the integral-SOR method and (b) the integral-spectral method.

obtained, either directly in the model's terrain-following coordinate system or indirectly (via vertical interpolations) in a local Cartesian coordinate system.

The main analysis domain, called domain D_1, comprises the entire domain shown in Fig. 2. Strong westerly winds blow into domain D_1 from its western boundary and prevail over most areas of domain D_1. The complexity of this original v field is evidenced by its sharp spatial variations and rapid flow pattern transitions from strongly divergent areas to strongly convergent areas (and vice versa) accompanied with conspicuous horizontal shears and/or rotations. At least four banded areas or belts of strong convergent flow can be clearly and easily identified and used for visual comparisons performed later in section 4. These four areas consist of two strong convergence zones accompanied with sharp wind direction changes (as shown by the two banded areas marked by Z1 and Z3 with orange boundaries in Fig. 2) and two with sharp wind speed changes (as shown by the two belt areas marked by Z2 and Z4 with yellow boundaries in Fig. 2).

Within the main analysis domain, two subdomains, called domains D_2 and D_3, are selected and will be used, in addition to domain D_1, for the test experiments in section 4. These two subdomains are shown in Fig. 2 by the rectangular areas within the dashed boundary lines colored in green (for D_2) and blue (for D_3). The two strong convergence zones, Z1 and Z2, are mostly contained in domain D_2, although Z1 extends beyond the eastern boundary and Z2 extends slightly beyond the western boundary of domain D_2. Another two strong convergence zones, Z3 and Z4, are
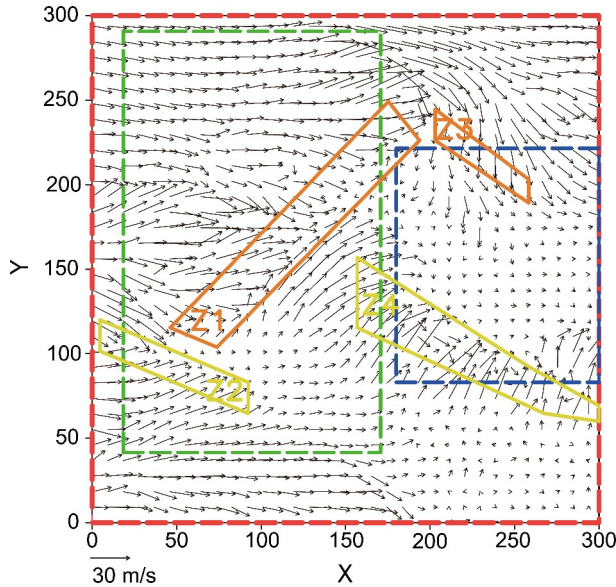

Fig. 2. Original v plotted by black arrows on the model's terrain-following vertical level about 0.5 km above the ground. The boundaries of the domains D_1, D_2, and D_3 are marked by red, green, and blue dashed lines, respectively. Convergence zones accompanied by sharp changes in wind direction and speed are enclosed by orange and yellow lines, respectively. The (x, y) coordinate origin is at the southwestern corner, and the (x, y) coordinates are marked/labeled every 50 km. The velocity scale is shown at the lower-left corner.

mostly contained in domain D_3, although the Z3 zone extends beyond the northern boundary, and the Z4 zone extends beyond the southern and western boundaries of domain D_3. Clearly, the original v field has sharp variations with strong convergence not only within each subdomain but also across or along some (or large) portions of the boundary of subdomain D_2 (or D_3). Thus, accurate computation of (ψ, χ) becomes increasingly difficult as the analysis domain is reduced from D_1 to D_2 and further reduced to D_3, as seen later from the results of test experiments in section 4.

3.2. *Evaluation methods*

Since the true values of (ψ, χ) are neither exactly known nor given in real cases, evaluations and verifications can be performed only by comparing the reconstructed horizontal velocity [denoted by $v_c \equiv (u_c, v_c)$] with the original one [denoted by $v \equiv (u, v)$] for the purpose of achieving closeness between v_c to v. Quantitatively, the closeness of v_c to v can be measured in terms of a spatial correlation coefficient (SCC) and a relative root-mean-square difference (RRD) defined by

$$
\text{SCC} = \sum\nolimits_{i,j} \{[u_{c(i,j)} - U_c][u_{(i,j)} - U] + [v_{c(i,j)} - V_c]
$$
$$
[v_{(i,j)} - V]\}/(mn\sigma_c\sigma) , \tag{9a}
$$

$$
\text{RRD} = \left\{ \left[\sum\nolimits_{i,j} (u_{c(i,j)} - u_{(i,j)})^2 + (v_{c(i,j)} - v_{(i,j)})^2 \right] \right/
$$
$$
\left. \sum\nolimits_{i,j} [u_{(i,j)}^2 + v_{(i,j)}^2] \right\}^{1/2} . \tag{9b}
$$

Here, m and n are the numbers of grid points in x and y directions, respectively, inside of the domain, $\sum_{i,j}$ denotes the summation over i from 1 to m and j from 1 to n, U_c, V_c, U, and V are the mean values of u_c, v_c, u, and v, respectively, over the domain, and

$$
\sigma_c^2 = \sum\nolimits_{i,j} \{[u_{c(i,j)} - U_c]^2 + [v_{c(i,j)} - V_c]^2\}/mn , \tag{9c}
$$

$$
\sigma^2 = \sum\nolimits_{i,j} \{[u_{(i,j)} - U]^2 + [v_{(i,j)} - V]^2\}/mn . \tag{9d}
$$

A high SCC and small RRD indicate high accuracy of v_c and vice versa. A simple quantitative criterion for adequate accuracy will be used in this paper, which requires

$$
\text{SCC} > 0.98 \text{ and RRD} < 0.15 . \tag{10}
$$

4. Results of experiments

The SCC and RRD values between original v and reconstructed v_c from each method are listed for each domain in Table 1. Computational costs are also recorded to assess the efficiency of all methods. All five methods cost less than three seconds of CPU time in the three experiments. Without parallel computing, the SOR method costs the least CPU time. The integral method can be easily parallelized to

achieve extremely high computational efficiency. Thus, the integral method can be much more efficient than the iterative SOR method with parallel computing, especially when the number of grid points for the discretized domain becomes extremely large. Results for the main analysis domain D_1 (rows 2–6 of Table 1) show that the M-spectral (or SOR-based) method is the least (or second least) accurate, the integral and integral-spectral methods have about the same accuracy, and the integral-SOR method is most accurate among the five methods. In this case, the SOR-based (M-spectral) method fails marginally (badly) in retaining adequate accuracy according to the criterion in (10). In particular, as shown in Fig. 3a, v_c from the SOR-based method deviates significantly from v around the southwest corner (within the southwest quadrant) and along the eastern boundary of D_1 and also has notable deviations from v in Z2 and Z4. However, it can largely reproduce the complex convergent flow structures of v in Z1 and Z3. As shown in Fig. 3b, v_c from the M-spectral method has large and/or notable deviations from v in many areas nearly over the entire domain D_1, especially in Z1, Z3, and Z4. In contrast, v_c from the other three methods has almost the same flow structures and intensities as v, and the deviations are hardly visible and therefore not shown. All three methods have adequate accuracies.

As the analysis domain is reduced from D_1 to D_2, sharp variations of v are seen across or along slightly increased portions of domain boundary, as indicated by (ζ, α) plotted in Figs. 4c, d for domain D_2 versus (ζ, α) in Figs. 4a, b for domain D_1. In this case, the SOR-based method further falters as its accuracy is reduced significantly (see row 7 versus row 2 of Table 1). The M-spectral method also fails to retain adequate accuracy. However, its accuracy is slightly improved (see row 8 versus row 3 of Table 1). In contrast,

Table 1. The SCC and RRD value between the original v and reconstructed v_c from each listed method for each domain. See Eqs. (9a, b) for definitions of SCC and RRD. Bold fonts indicate those values where both SCC and RRD satisfy the accuracy adequacy criterion given by Eq. (10).

Domain	Method	SCC	RRD
D_1	SOR-based	0.9392	0.2820
	M-spectral	0.7836	0.5479
	Integral	**0.9870**	**0.1156**
	Integral-spectral	**0.9867**	**0.1151**
	Integral-SOR	**0.9958**	**0.0720**
D_2	SOR-based	0.8644	0.2641
	M-spectral	0.8661	0.3680
	Integral	**0.9809**	**0.1115**
	Integral-spectral	**0.9822**	**0.1032**
	Integral-SOR	**0.9932**	**0.0648**
D_3	SOR-based	0.8889	0.5024
	M-spectral	0.8753	0.5786
	Integral	0.9740	0.2240
	Integral-spectral	0.9633	0.2698
	Integral-SOR	**0.9909**	**0.1288**

the remaining three methods still have adequate accuracy, noting further that the integral-SOR method is still the most accurate (see rows 9–11 of Table 1). In particular, as shown in Fig. 3c, v_c from the SOR-based method has large deviations from v near the eastern boundary of domain D_2, especially at and around the northern tip of Z1 and the eastern end of Z4. In contrast, the complex convergent flow structures of v, especially those in the three convergent zones, are well captured by v_c from the integral method (Fig. 3d) and almost identically reproduced by v_c from the integral-SOR method (not shown).

As the analysis domain is further reduced to domain D_3, sharp variations of v are not only distributed across or along increased large portions of domain boundary but are also concentrated near the southern and northern boundaries as indicated by (ζ, α), as plotted in Figs. 4e, f. In this case, accuracy losses are seen to various degrees for all the methods (see results for D_3 versus those for D_2 in Table 1), but the integral-SOR method has the smallest accuracy loss and still maintains adequate accuracy. In contrast, the four remaining methods fail to retain adequate accuracy, and the M-spectral (SOR-based) method is still least (second least) accurate. In particular, as shown in Fig. 3e, v_c from the integral method has significant or large deviations from v in Z4 around the southwest corner and along large portions of southern and western boundaries of domain D_3. Still, these deviations are mostly corrected in terms of v_c from the integral-SOR method, as shown in Fig. 3f.

The accuracy of (ψ_{in}, χ_{in}) obtained from the first step of the integral method (also the first step of each hybrid method) is checked by comparing (ζ_c, α_c) with (ζ, α) computed from v, where ζ_c (or α_c) denotes the vorticity (or divergence) in terms of the reconstructed v_c and is computed here from $\nabla^2\psi_{in}$ (or $\nabla^2\chi_{in}$). As shown in Fig. 4, (ζ_c, α_c) matches (ζ, α) almost perfectly in domain D_1, although the closeness of (ζ_c, α_c) to (ζ, α) decreases slightly as the analysis domain reduces from D_1 to D_2 and then to D_3. In contrast, when (ζ_c, α_c) is computed from $\nabla^2(\psi_{in,n}, \chi_{in,n})$, with $(\psi_{in,n}, \chi_{in,n})$ obtained from the first step of M-spectral method, the computed (ζ_c, α_c) matches (ζ, α) very poorly in each domain (not shown). This implies that $(\psi_{in,n}, \chi_{in,n})$ is not accurately computed, as its computation is sensitive to the effects of the complex flow structures of v in each domain. Besides, the use of homogeneous boundary conditions in the first step of the M-spectral method causes sharp cross-boundary variations of $(\psi_{in,n}, \chi_{in,n})$ and even sharper cross-boundary variations of (ζ_c, α_c) computed from $\nabla^2(\psi_{in,n}, \chi_{in,n})$, and this also partially explains the aforementioned poor match.

The left-hand-side and right-hand-side terms of the solvability conditions in Eqs. (3a) and (3b) are computed by using v in each domain. The computed values are listed in each row of Table 2, showing that these two solvability conditions are satisfied accurately by v (as stated earlier in section 2). The left-hand-side terms of the solvability conditions in Eqs. (3a) and (3b) are also computed in each domain by using the v_c values from each method. These computed values
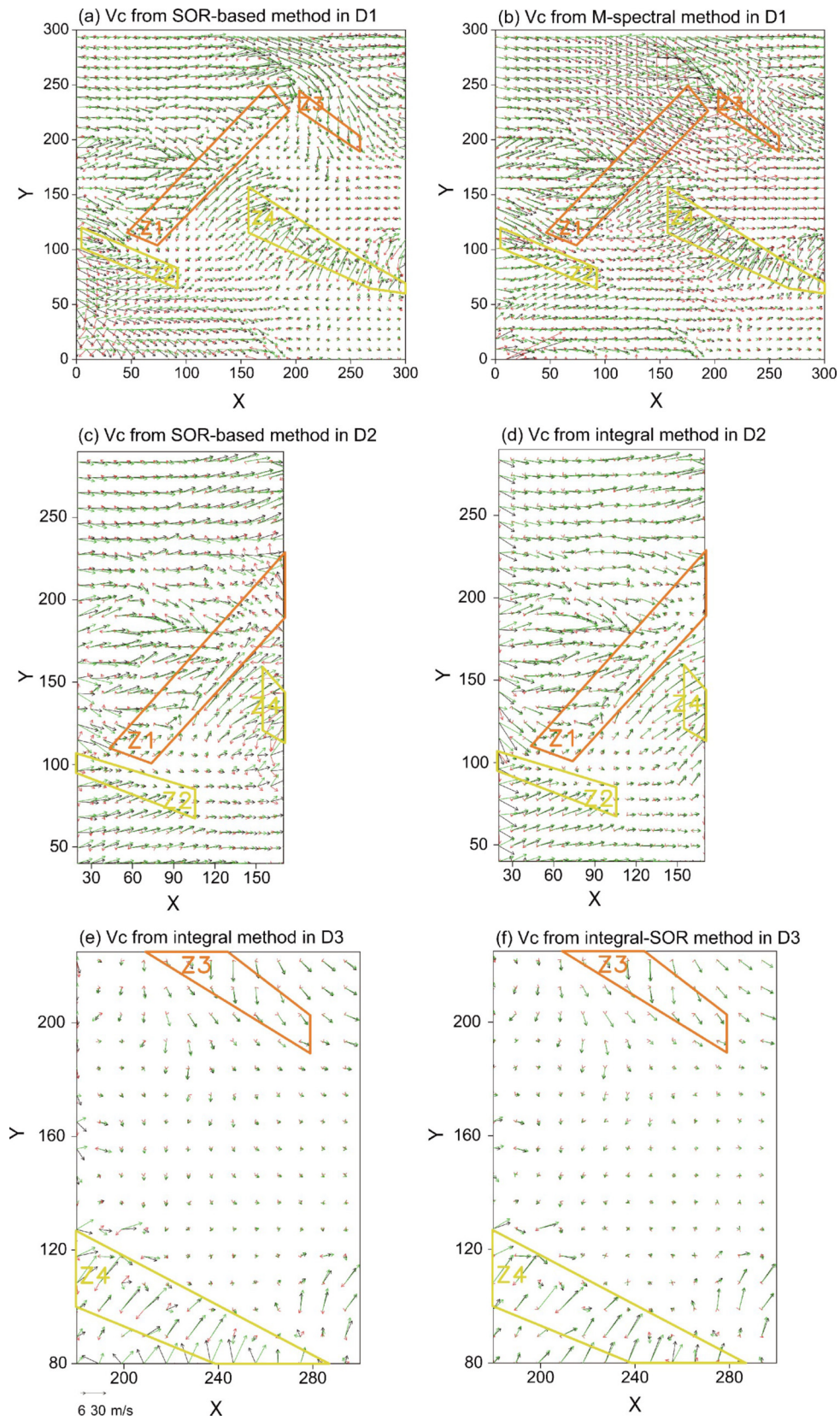
Fig. 3. Reconstructed velocity v_c (plotted by black arrows) overlaid by original velocity v (plotted by green arrows) and velocity difference $v_c - v$ (plotted by red arrows) in the domain D_1 from (a) the SOR-based method and (b) the M-spectral method, and in domain D_2 from (c) the SOR-based method and (d) the integral method, and in domain D_3 from (e) the integral method and (f) the integral-SOR method.
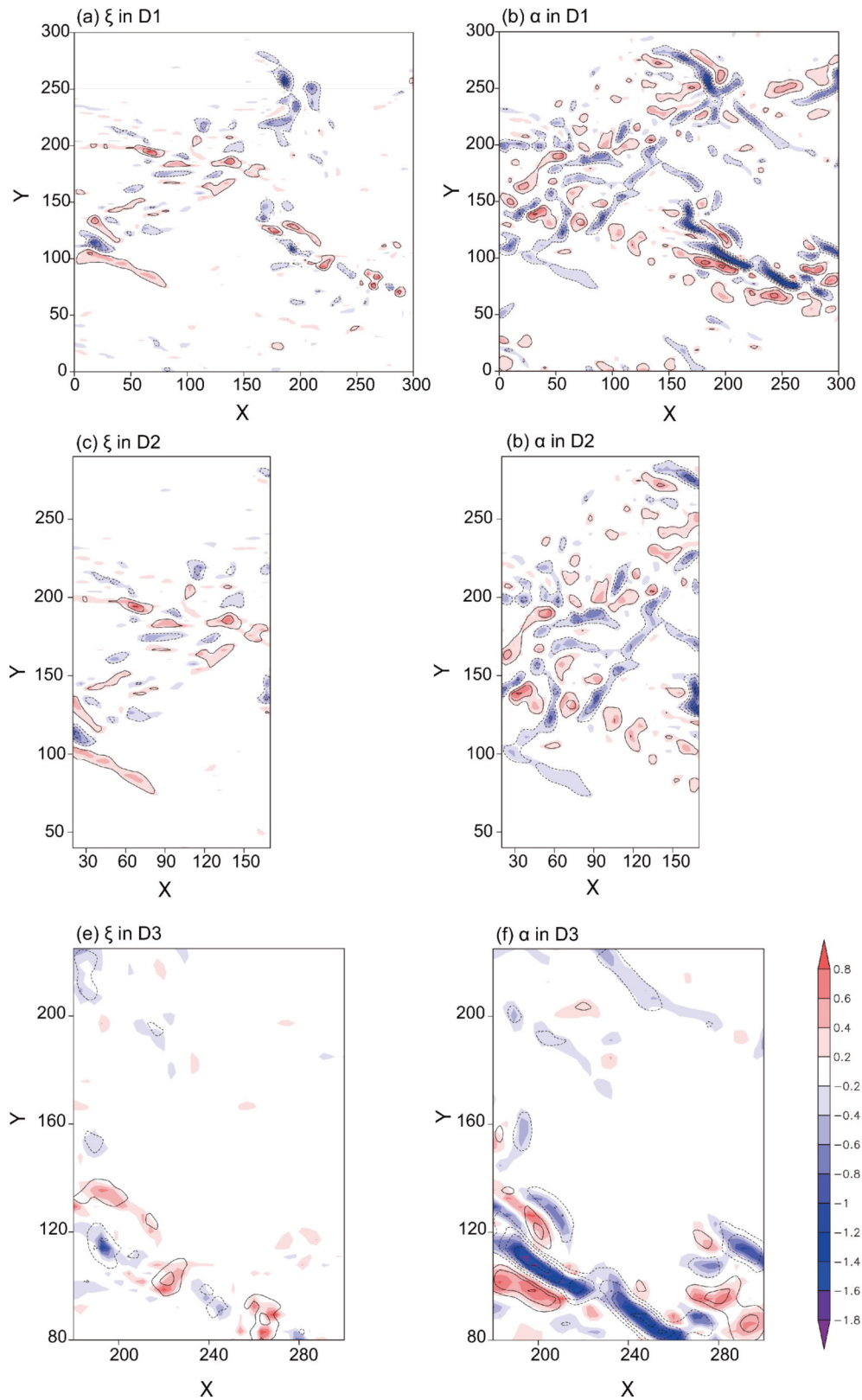
Fig. 4. Reconstructed ζ_c (or α_c) plotted by black contours (every 2×10^{-4} s^{-1}) versus original ζ (or α) shown by color shades in the top left (or right) panel for domain D_1, middle left (or right) panel for domain D_2, and bottom left (or right) panel for domain D_3. Here, ζ (or α) is computed from original v. At the same time, ζ_c (or α_c) denotes the vorticity (or divergence) of reconstructed v_c and is computed here from $\nabla^2 \psi_{in}$ (or $\nabla^2 \chi_{in}$) with (ψ_{in}, χ_{in}) obtained from the first step of the integral method (that is also the first step of each hybrid method). The color scale is shown on the right side in the last panel.

are then normalized by the corresponding values computed by using $\boldsymbol{v}$ in the same domain. As listed in Table 3, the normalized values deviate from one to different percentages for different methods, indicating that the two solvability conditions are not accurately satisfied by $\boldsymbol{v}_c$ —again, as previously stated in section 2. In particular, large or very large deviations are seen for the three previous methods. In comparison, relatively small to very small deviations are seen for the two hybrid methods, especially the integral-SOR method. Note that $\boldsymbol{v}_e \equiv \boldsymbol{k} \times \nabla\psi_e + \nabla\chi_e = \boldsymbol{k} \times \nabla\psi_e$ is the externally induced component obtained with $\chi_e = 0$ in the second step of either the integral or integral-SOR method, so its contribution to $\int_S v_n dl$ is $-\int_S \partial_s \psi_e \, dl = -\int_S d\psi_e = 0$ and its contribution to $\int_S v_s dl$ is $\int_S \partial_n \psi_e dl$ and is not exactly zero (as it should be) and deviates from zero differently for the two (integral and integral-SOR) methods. This explains why the integral and integral-SOR methods have the same normalized value for $\int_S v_n dl$ but not for $\int_S v_s dl$, as shown in Table 3. Table 4 lists the normalized values of $\int_S v_{s,in} dl$ and $\int_S v_{n,in} dl$ with $(v_{s,in}, v_{n,in})$ obtained from the first step of the integral method. For each domain, the nor-

Table 2. Values of the left-hand-side and right-hand-side terms of solvability conditions in Eqs. (3a) and (3b) computed by using the original $\boldsymbol{v}$ in each domain are listed in each row (units: 10^{-5} m^2 s^{-1}) .

Domain	$\int_S v_s ds$	$\int_D \zeta d\boldsymbol{x}$	$\int_S v_n dl$	$\int_D \alpha d\boldsymbol{x}$
D_1	−10.5308	−10.5308	−10.8613	−10.8613
D_2	2.6230	2.6230	−6.7034	−6.7034
D_3	−1.9023	−1.9023	−13.8323	−13.8323

Table 3. Normalized values of the left-hand-side terms of solvability conditions in Eqs. (3a) and (3b) computed with (v_s, v_n) given by $\boldsymbol{v}_c$ in each domain from each method are listed in each row. The values of $\int_S v_s dl$ from the five methods listed for each domain are normalized by the value of $\int_S v_s dl$ listed for the same domain in Table 2. The values of $\int_S v_s dl$ from the five methods listed for each domain are normalized by the value of $\int_S v_n dl$ listed for the same domain in Table 2.

Domain	Method	$\int_S v_s dl$	$\int_S v_n dl$
D_1	SOR-based	0.9852	0.5884
	M-spectral	1.7570	1.0915
	Integral	1.1236	1.0047
	Integral-SOR	0.9973	1.0047
	Integral-spectral	0.9868	1.0757
D_2	SOR-based	0.8368	0.4332
	M-spectral	0.5385	1.4400
	Integral	1.7196	0.8844
	Integral-SOR	0.9247	0.8844
	Integral-spectral	0.8302	0.9090
D_3	SOR-based	0.7653	0.4765
	M-spectral	0.7808	1.1484
	Integral	0.6659	0.9457
	Integral-SOR	0.9812	0.9457
	Integral-spectral	0.8176	0.9693

malized value of $\int_S v_{n,in} dl$ in Table 4 is identical to that of $\int_S v_n dl$ from the integral (or integral-SOR) method in Table 3. This is again due to the above-explained zero contribution of $\boldsymbol{v}_e$ to $\int_S v_n dl$. However, starting from the normalized value of $\int_S v_{s,in} dl$ in Table 4 for each domain, the normalized value of $\int_S v_s dl$ from the integral method in Table 3 deviates further or even much further away from one, and this is due mainly to relatively larger errors in $\boldsymbol{v}_e$ obtained from the second step of the integral method—which is sensitive to small errors in boundary conditions as explained earlier in section 2.1. Judging from the closeness of normalized value to one from each method listed in Table 3 for each domain, the integral-SOR method is still the most accurate among the five methods.

Boundary conditions are of vital importance for mesoscale diagnostic studies and numerical modeling. Table 3 gives an averaged evaluation of $\boldsymbol{v}_c$ accuracy from each method along the four boundaries of each domain. Judging from the closeness of normalized value to one listed in Table 3 from each method for each domain, the integral method and two hybrid methods are more accurate than the other two. Figure 5 depicts the along-boundary distributions of the original v_s (v_n) versus reconstructed v_s (v_n) to reveal detailed resemblances and discrepancies between $\boldsymbol{v}$ and $\boldsymbol{v}_c$ along the four boundaries of each domain. The complex variations and local extrema of the original (v_s, v_n) are well captured by the reconstructed (v_s, v_n) from the two hybrid methods (shown by the orange and red curves in Fig. 5) but not well captured by the other three methods. The integral method captures v_n very closely because the externally induced part of v_n, i.e., $-\partial_s \psi_e$, is computed purely and quite accurately from the boundary condition of ψ_e (obtained by integrating $v_{n,in} - v_n$ as explained in section 2.1), but it fails badly in capturing v_s due mainly to large errors in $\boldsymbol{v}_e$ obtained from the second step of the integral method (again as explained earlier in section 2.1).

5. Conclusions

This paper reveals, for the first time, that all three types of methods previously used for computing the streamfunction ψ and the velocity potential χ in limited domains fail to retain adequate accuracies to different degrees when applied to complex flows with near grid scales in limited domains. This is indicated by the failures of computed ψ and χ to reconstruct the original horizontal velocity $\boldsymbol{v}$ to adequate accuracies. This modeling aspect represents a new problem encoun-

Table 4. As in Table 3, but computed with $(v_{s,in}, v_{n,in})$ given by the internally-induced component of $\boldsymbol{v}_c$ in each domain obtained from the first step of the integral method listed in each row.

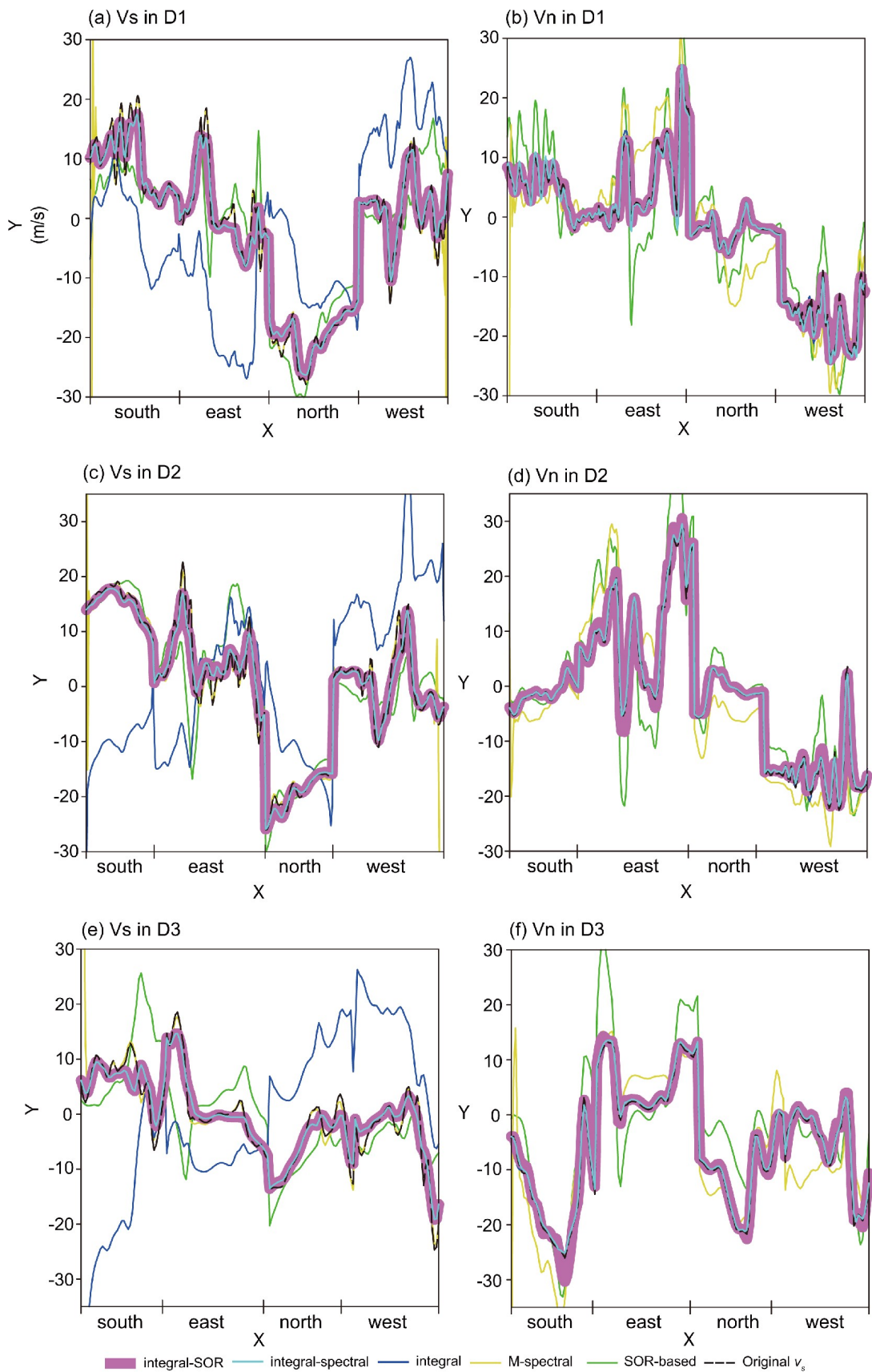| Domain	$\int_S v_{s,in} dl$	$\int_S v_{n,in} dl$
D_1	0.9725	1.0047
D_2	0.9421	0.8844
D_3	0.7188	0.9457

Fig. 5. The original v_s (or v_n) plotted in dashed black versus the reconstructed v_s (or v_n) plotted in solid green for the SOR-based method, yellow for M-spectral method, blue for integral method, orange for integral-spectral method, and red for integral-SOR method along four boundaries of domain D_1 in top-left (or right) panel, domain D_2 in middle-left (or right) panel, and domain D_3 in bottom-left (or right) panel.

tered in our recent application of previous numerical methods to complex flows. The numerical issue yields sharp horizontal variations not only inside each domain but also across or along large portions of the domain boundary. This problem cannot be solved by simply interpolating the original flow field into a finer mesh because the interpolated field still cannot resolve the complex flow structures that are either unresolved or poorly resolved by the original field, considering that the spatial resolution of the original flow field is predetermined by its data source (from a model output or reanalysis).

To solve this problem, we revisit three types of previous methods (in sections 2.1–2.3) to identify and/or envision each method's strengths and key weaknesses, which ultimately causes a significant loss of accuracy when applied to complex flows over mesoscale domains. In particular, the SOR-based method (Sangster, 1960) and the spectral method (CK92b, but modified with a well-redefined inner solution as shown in section 2.3) are found to lose their accuracies mainly in response to increased spatial variations of v inside the limited domain, while their accuracies are not affected much by increased variations of v across or along the domain boundary. Increasing the number of iterative steps fails to reduce the errors caused by their inherent weaknesses. On the contrary, the integral method (CX11) is found to lose its accuracy mainly in response to increased variations of v across and along the domain boundary, which reduces the accuracy of the externally induced (ψ, χ) obtained in the second step while retaining sufficient accuracy obtained in the first step for the internally induced (ψ, χ), despite the increased spatial variations of v inside the domain.

Based on the above findings, two hybrid methods are developed optimally by combining the strengths of the previously mentioned methods (in section 2.4). One is called the integral-SOR method, which combines the first step of the integral method with the second step adopted from the SOR-based method. The other is called the integral-spectral method, which combines the first step of the integral method with the second step adopted from the spectral method. These two hybrid methods are tested against the three previous methods with real-case, complex flows over three mesoscale domains with successively reduced domain sizes (see section 3.1). The accuracy of each method is measured and evaluated by the spatial correlation coefficient and the relative root-mean-square difference between v and its corresponding reconstructed one in each domain (see section 3.2). The test results show that the integral-SOR method is significantly more accurate than the integral-spectral method. At the same time, the integral-spectral method is generally more accurate than the three previous methods. However, the integral method (the most accurate among the three previous methods) is slightly more accurate than the integral-spectral method for the smallest domain. Computational costs are investigated in the three experiments. All five methods cost similar CPU time (less than 3 seconds),

and the SOR method costs the least without parallel computing. For future applications to domains with massive grid points, parallel computing can easily be adopted to greatly increase the computational efficiency for the integral and hybrid methods. Therefore, the integral-SOR method is recommended for future applications and diagnostic studies of complex flows over mesoscale domains.

REFERENCES

Aimi, A., G. Buffoni, and M. Groppi, 2014: Decomposition of a planar vector field into irrotational and rotational components. *Applied Mathematics and Computation*, **244**, 63–90, https://doi.org/10.1016/j.amc.2014.06.080.

Allen, J. S., J. A. Barth, and P. A. Newberger, 1990: On intermediate models for barotropic continental shelf and slope flow fields. *Part I: Formulation and Comparison of Exact Solutions. J. Phys. Oceanogr.*, **20**, 1017–1042, https://doi.org/10.1175/1520-0485(1990)020<1017:OIMFBC>2.0.CO;2.

Boyd, J. P., D. F. Deng, Q. S. Chen, and S. T. Gao, 2013: Applications of bivariate fourier series for solving the Poisson equation in limited-area modeling of the atmosphere: Higher accuracy with a boundary buffer strip discarded and an improved order-raising procedure. *Mon. Wea. Rev.*, **141**, 4154–4164, https://doi.org/10.1175/MWR-D-13-00074.1.

Buechler, D. E., and H. E. Fuelberg, 1986: Budgets of divergent and rotational kinetic energy during two periods of intense convection. *Mon. Wea. Rev.*, **114**, 95–114, https://doi.org/10.1175/1520-0493(1986)114<0095:BODARK>2.0.CO;2.

Cao, J., 2021: Computing streamfunction and velocity potential

near the Tibetan Plateau. *Atmospheric Research*, **247**, 105149, https://doi.org/10.1016/j.atmosres.2020.105149.

Cao, J., and Q. Xu, 2011: Computing streamfunction and velocity potential in a limited domain of arbitrary shape. Part II: Numerical methods and test experiments. *Adv. Atmos. Sci.*, **28**, 1445−1458, https://doi.org/10.1007/s00376-011-0186-5.

Cao, Z. H., Q. Xu, and D. L. Zhang, 2019: A new method to diagnose cyclone-cyclone interaction and its influences on precipitation. *J. Appl. Meteor. Climatol.*, **58**, 1821−1851, https://doi.org/10.1175/JAMC-D-18-0344.1.

Chen, Q. S., and Y. H. Kuo, 1992a: A harmonic-sine series expansion and its application to partitioning and reconstruction problems in a limited area. *Mon. Wea. Rev.*, **120**, 91−112, https://doi.org/10.1175/1520-0493(1992)120<0091:AHSSEA>2.0.CO;2.

Chen, Q. S., and Y. H. Kuo, 1992b: A consistency condition for wind-field reconstruction in a limited area and a harmonic-cosine series expansion. *Mon. Wea. Rev.*, **120**, 2653−2670, https://doi.org/10.1175/1520-0493(1992)120<2653:ACCFWF>2.0.CO;2.

Daley, R., 1991: *Atmospheric Data Analysis*. Cambridge University Press, 457 pp.

DiMego, G. J., and L. F. Bosart, 1982: The transformation of tropical storm Agnes into an extratropical cyclone. Part I: The observed fields and vertical motion computations. *Mon. Wea. Rev.*, **110**, 385−411, https://doi.org/10.1175/1520-0493(1982)110<0385:TTOTSA>2.0.CO;2.

Fiedler, B. H., 2002: A wind transform for acoustic adjustment in compressible models. *Mon. Wea. Rev.*, **130**, 741−746, https://doi.org/10.1175/1520-0493(2002)130<0741:AWTFAA>2.0.CO;2.

Fu, S. M., S. L. Jin, W. Shen, D. Y. Li, B. Liu, and J. H. Sun, 2021: A kinetic energy budget on the severe wind production that causes a serious state grid failure in southern Xinjiang China. *Atmospheric Science Letters*, **21**, e977, https://doi.org/10.1002/asl.977.

Haltiner, G. J., and R. T. Williams, 1980: *Numerical Prediction and Dynamic Meteorology*. 2nd ed., John Wiley & Sons, 477 pp.

Hollingsworth, A., and P. Lönnberg, 1986: The statistical structure of short-range forecast errors as determined from radiosonde data. Part I: The wind field. *Tellus A: Dynamic Meteorology and Oceanography*, **38**, 111−136, https://doi.org/10.3402/tellusa.v38i2.11707.

Jung, J. H., and A. Arakawa, 2008: A three-dimensional anelastic model based on the vorticity equation. *Mon. Wea. Rev.*, **136**, 276−294, https://doi.org/10.1175/2007MWR2095.1.

Li, Z. J., Y. Chao, and J. C. McWilliams, 2006: Computation of the streamfunction and velocity potential for limited and irregular domains. *Mon. Wea. Rev.*, **134**, 3384−3394, https://doi.org/10.1175/MWR3249.1.

Loughe, A. F., C. C. Lai, and D. Keyser, 1995: A technique for diagnosing three-dimensional ageostrophic circulations in baroclinic disturbances on limited-area domains. *Mon. Wea. Rev.*, **123**, 1476−1504, https://doi.org/10.1175/1520-0493(1995)123<1476:ATFDTD>2.0.CO;2.

Lynch, P., 1989: Partitioning the wind in a limited domain. *Mon. Wea. Rev.*, **117**, 1492−1500, https://doi.org/10.1175/1520-0493(1989)117<1492:PTWIAL>2.0.CO;2.

Ma, S. P., L. K. Ran, and J. Cao, 2021: Diagnosis and analysis of vertical motion during complex topographical heavy snowfall. *Chinese Journal of Atmospheric Sciences*, **45**, 1127−1145, https://doi.org/10.3878/j.issn.1006-9895.2105.20206. (in Chinese with English abstract)

Mewes, J. J., and A. Shapiro, 2002: Use of the vorticity equation in dual-Doppler analysis of the vertical velocity field. *J. Atmos. Ocean. Technol. 19*(5), 543−567, https://doi.org/10.1175/1520-0426(2002)019<0543:UOTVEI>2.0.CO;2.

Parrish, D. F., and J. C. Derber, 1992: The national meteorological center's spectral statistical-interpolation analysis system. *Mon. Wea. Rev.*, **20**, 1747−1763, https://doi.org/10.1175/1520-0493(1992)120<1747:TNMCSS>2.0.CO;2.

Sangster, W. E., 1960: A method of representing the horizontal pressure force without reduction of station pressures to sea level. *J. Meteor.*, **17**, 166−176, https://doi.org/10.1175/1520-0469(1960)017<0166:AMORTH>2.0.CO;2.

Ullah, W., G. J. Wang, Z. Q. Gao, D. F. T. Hagan, A. S. Bhatti, and C. Zhua, 2020: Observed Linkage between Tibetan Plateau soil moisture and South Asian summer precipitation and the possible mechanism. *J. Climate*, **34**, 361−377, https://doi.org/10.1175/JCLI-D-20-0347.1.

Ullah, W., and Coauthors, 2021: Large-scale atmospheric circulation patterns associated with extreme monsoon precipitation in Pakistan during 1981-2018. *Atmospheric Research*, **232**, 105489, https://doi.org/10.1016/j.atmosres.2021.105489.

Vallis, G. K., G. J. Shutts, and M. E. B. Gray, 1997: Balanced mesoscale motion and stratified turbulence forced by convection. *Quart. J. Roy. Meteor. Soc.*, **123**, 1621−1652, https://doi.org/10.1002/qj.49712354209.

Xu, Q., 2021: A variational method for analyzing vortex flows in radar-scanned tornadic mesocyclones. Part I: Formulations and theoretical considerations. *J. Atmos. Sci.*, **78**, 825−841, https://doi.org/10.1175/JAS-D-20-0158.1.

Xu, Q., and C. J. Qiu, 1994: Simple adjoint methods for single-Doppler wind analysis with a strong constraint of mass conservation. *J. Atmos. Ocean. Technol.*, **11**, 289−298, https://doi.org/10.1175/1520-0426(1994)011<0289:SAMFSD>2.0.CO;2.

Xu, Q., and L. Wei, 2001: Estimation of three-dimensional error covariances. Part II: Analysis of wind innovation vectors. *Mon. Wea. Rev.*, **129**, 2939−2954, https://doi.org/10.1175/1520-0493(2001)129<2939:EOTDEC>2.0.CO;2.

Xu, Q., and L. Wei, 2002: Estimation of three-dimensional error covariances. Part III: Height-wind forecast error correlation and related geostrophy. *Mon. Wea. Rev.*, **130**, 1052−1062, https://doi.org/10.1175/1520-0493(2002)130<1052:EOTDEC>2.0.CO;2.

Xu, Q., S. Liu, and M. Xue, 2006: Background error covariance functions for vector wind analyses using Doppler radar radial-velocity observations. *Quart. J. Roy. Meteor. Soc.*, **132**, 2887−2904, https://doi.org/10.1256/qj.05.202.

Xu, Q., K. Nai, and L. Wei, 2007: An innovation method for estimating radar radial-velocity observation error and background wind error covariances. *Quart. J. Roy. Meteor. Soc.*, **133**, 407−415, https://doi.org/10.1002/qj.21.

Xu, Q., and J. Cao, 2021: Iterative methods for solving the nonlinear balance equation with optimal truncation. *Adv. Atmos. Sci.*, **38**(5), 755−770, https://doi.org/10.1007/s00376-020-0291-4.

Xu, Q., J. Cao, and S. T. Gao, 2011: Computing streamfunction and velocity potential in a limited domain of arbitrary shape.

Part I: Theory and integral formulae. *Adv. Atmos. Sci.*, **28**, 1433–1444, https://doi.org/10.1007/s00376-011-0185-6.

You, C., and J. C. H. Fung, 2019: Characteristics of the Sea-Breeze circulation in the Pearl River Delta Region and its dynamical diagnosis. *J. Appl. Meteor. Climatol.*, **58**, 741–755, https://doi.org/10.1175/JAMC-D-18-0153.1.

You, C., J. C. H. Fung, and W. P. Tse, 2019: Response of the Sea Breeze to urbanization in the Pearl River delta region. *J. Appl. Meteor. Climatol.*, **58**, 1449–1463, https://doi.org/10.1175/JAMC-D-18-0081.1.

Zhao, S. Y., and K. H. Cook, 2021: Influence of Walker circulations on East African rainfall. *Climate Dyn.*, **7**, 2127–2147, https://doi.org/10.1007/s00382-020-05579-7.